

High-refractive index and mechanically cleavable non-van der Waals InGaS₃

A. N. Toksumakov^{1,2}, G. A. Ermolaev¹, A. S. Slavich¹, N. V. Doroshina¹, E. V. Sukhanova², D. I. Yakubovsky¹, S. M. Novikov¹, A. S. Oreshonkov³, D. M. Tsymbarenko⁴, Z. I. Popov², D. G. Kvashnin², A. A. Vyshnevyy¹, A. V. Arsenin^{1,5}, D. A. Ghazaryan^{1,*} and V. S. Volkov^{1,5,*}

¹Center for Photonics and 2D Materials, Moscow Institute of Physics and Technology, Dolgoprudny 141701, Russia

²Emanuel Institute of Biochemical Physics RAS, Moscow 119334, Russia

³School of Engineering and Construction, Siberian Federal University, Krasnoyarsk 660041, Russia

⁴Department of Chemistry, Lomonosov Moscow State University, Moscow 119991, Russia

⁵XPANCEO, Moscow 127495, Russia

*Authors to whom correspondence should be addressed: kazarian.da@mipt.ru and volkov.vs@mipt.ru

Abstract

The growing families of two-dimensional crystals derived from naturally occurring van der Waals materials offer an unprecedented platform to investigate elusive physical phenomena and could be of use in a diverse range of devices. Of particular interest are recently reported atomic sheets of non-van der Waals materials, which could allow a better comprehension of the nature of structural bonds and increase the functionality of prospective heterostructures. Here, we study the optostructural properties of ultrathin non-van der Waals InGaS₃ sheets produced by standard mechanical cleavage. Our ab initio calculation results suggest an emergence of authentically delicate out-of-plane covalent bonds within its unit cell, and, as a consequence, an artificial generation of layered structure within the material. Those yield to singular layer isolation energies of $\sim 50 \text{ meV}\text{\AA}^{-2}$, which is comparable with the conventional van der Waals material's monolayer isolation energies of 20 - 60 $\text{meV}\text{\AA}^{-2}$. In addition, we provide a comprehensive analysis of the structural, vibrational, and optical properties of the materials presenting that it is a wide bandgap (2.73 eV) semiconductor with a high-refractive index (> 2.5) and negligible losses in the visible and infrared spectral ranges. It makes it a perfect candidate for further establishment of visible-range all-dielectric nanophotonics.

Introduction

Research on layered materials with relatively weak out-of-plane van der Waals bonds is of great significance nowadays. These layered materials are studied in natural^{1,2} and artificial heteroformations³⁻⁶. Accounting for their stoichiometric composition and crystal structure, one can classify the former into graphene, transition metal dichalcogenide or mono- chalcogenide, sulfosalt, oxide, neo-, phyllo- silicate and phosphate families. The latter is assembled physically by stacking

atomic layers with strong in-plane covalent bonds of the former on top of each other^{3,7}. In addition, one can also introduce a nominal categorization for such layered materials based on their cleavage feasibility into separate atomic sheets⁸. It could be understood as an energy required for the isolation or separation of a singular atomic layer from the bulk^{9,10}. In first-principles calculations, the interlayer binding energy per unit area is a key parameter that determines the probability of such an event. Within this formalism, it is reasonable to distinguish naturally, potentially cleavable, and robust materials with threshold exfoliation energies of the order of magnitudes of⁸ 10 meVÅ⁻², 100 meVÅ⁻², and 1000 meVÅ⁻², respectively. Apart from natural van der Waals formations, some of the cleavable materials lack the out-of-plane van der Waals bonds in their structure. They form interlayer bonds of a different nature, e.g., covalent, but of comparable strengths and bear the name of non-van der Waals materials¹¹⁻¹⁸. Vivid examples attained on probation are atomic sheets of Fe₂O₃¹⁵, AgCrS₂¹⁶ and FeS₂¹⁹, derived through sonication-assisted and cation-intercalation exfoliation methods, respectively.

In this article, we explore the optostructural properties of the hexagonal phase of InGaS₃ expanding the list of non-van der Waals materials. We demonstrate that unlike orthorhombic InGaS₃ predicted theoretically²⁰, its hexagonal phase obeys a non-layered arrangement of crystal structure. Peculiarly, it can be cleaved down to atomically thin sheets due to the presence of few and delicate out-of-plane bonds within its unit cell. Our findings are based on systematic study of the crystal lattice through X-ray crystallography and supported by first-principles calculations. In addition, we demonstrate an alternative crystal structure reckoning technique combining the spectroscopic ellipsometry with first-principles calculations. It allows us to resolve that the hexagonal InGaS₃ is a wide bandgap (2.73 eV) semiconductor with high-refractive index (> 2.5) and negligible losses for visible and infrared spectra, which makes it relevant for next-generation nanophotonics and mietronics.

Results

Structure and morphology of non-van der Waals InGaS₃

Typical crystals of InGaS₃ appear with yellow-to-lustrous grey shades as displayed in Figure 1 (a). Such colours are determined by the 1:1:3 ratio distribution of Indium: Gallium: Sulphur atoms (see energy-dispersive X-ray spectroscopy pattern in Supplementary Figure S1). The crystals exhibit a hexagonal arrangement of III-III-IV group elements in the P6₅ space group with lattice parameters of $a = b = 6.6$ Å and $c = 17.9$ Å as presented in the inset of Figure 1 (a). Our all-through crystallographic imaging results confirm its hexagonal structure. Figure 1 (b and c) demonstrate the selected X-ray diffraction patterns across two eminent a^*b^* and c^*b^* crystallographic planes. Notably, a similar hexagonal structure of InGaS₃ was previously reported with a high R -value, 8.1 %, in the chiral P6₁ space group²¹. However, testing the space group for the dataset collected from our samples resulted in an unsatisfactory Flack's parameter of 0.94 (3) imposing a requirement for swapping within an enantiomorphic pair, P6₁ -> P6₅²². Further details on data collection, refinement parameters and interatomic distances are provided in Methods and Supplementary Tables ST1, ST2. In addition, the hexagonal structure of the material was alternatively verified through transmission electron microscopy (see Supplementary Figure S2 for diffraction pattern across a^*b^* crystallographic plane reflex interpretations).

The hexagonal InGaS₃ contains various structural bonds, whose strengths were estimated by first-principles calculations based on density functional theory (DFT). To obtain energies required for the

isolation of individual atomic sheets, we estimated the differences among the ground-state energy of the relaxed structure and all of its unrelaxed states. Afterwards, we looked for the planes with the minimal binding energies to determine potentially breakable, or in our case, cleavable directions. Excluding relaxation energies along the c -axis, we found the exfoliation energy of $E_{\text{exf}} \approx 53 \text{ meV}\text{\AA}^{-2}$ for the planes shown in Figure 1 (d). After accounting for the further relaxation of such isolated layers²³, we obtained an even smaller exfoliation energy of $E_{\text{exf}}^* \approx 21 \text{ meV}\text{\AA}^{-2}$. Figure 1 (e) compares our results with the evaluated exfoliation energies of conventional van der Waals (and non-van der Waals) materials. Notably, the energies of conventional van der Waals materials cover the range of 20 to 60 $\text{meV}\text{\AA}^{-2}$, unlike for non-van der Waals ones with a larger dispersion in the range of 25 to 180 $\text{meV}\text{\AA}^{-2}$. Our InGaS_3 has relatively low exfoliation energy among other non-van der Waals materials, which is slightly lower than that of some van der Waals materials, such as PdS_2 and PdSe_2 .

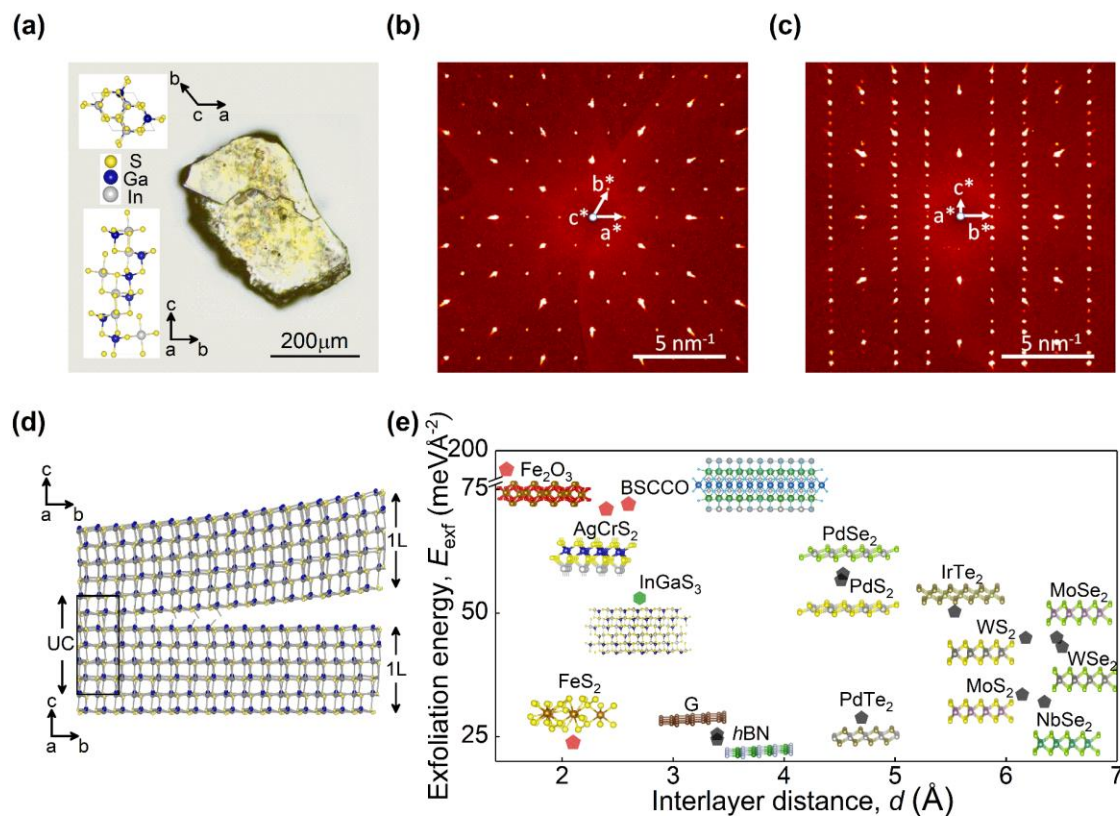


Figure 1: Crystal structure and interplane binding energies of non-van der Waals InGaS_3 . **a** 5X optical micrograph of bulk crystal on a glass slide. Inset: Top and side views of $P6_5$ space group hexagonal crystal structure with lattice constants of $a = b = 6.6 \text{ \AA}$, $c = 17.9 \text{ \AA}$. The a , b , c and a^* , b^* , c^* correspondingly introduce real and reciprocal space axes throughout the figure. **b** X-ray diffraction micrograph of the crystal presented in panel (a) across a^*b^* -plane. **c** Same as (b), but across c^*b^* -plane. **d** Schematic representation of artificially generated layered structure achieved by cutting off the delicate non-van der Waals bonds. UC stands for unit cell, 1L for artificially created monolayer. **e** Typical exfoliation energies of conventional van der Waals (black pentagons) and non-van der Waals (red pentagons) materials evaluated by first-principles calculations. Green hexagon presents our evaluation of the exfoliation energy along the proposed minimal energy atomic plane.

Slightly elevated temperature treatment within the standard exfoliation procedure⁷ allows the cleavage of InGaS_3 crystals into individual nanosheets with smooth surfaces (see Figure 2(a)). In contrast, the ultrathin atomic sheets preserve their flatness to a certain extent (see Supplementary Figure S3 for atomic-force micrographs of inhomogeneous atomic sheets). This is attributed to the

lack of apparent layered structure with out-of-plane van der Waals bonds within the material. We presume that the inhomogeneous sheets are obtained owing to the arbitrary breakage of some of the other, less delicate, non-van der Waals bonds within the material. Figure 2 (b-d) show AFM scans of pristine atomic sheets with nearly atomically flat surfaces (root-mean-square roughness of 0.3 nm). Thicknesses of these sheets correspond to one (1L), two (2L), three (3L), four (4L) and five (5L) artificially generated monolayers.

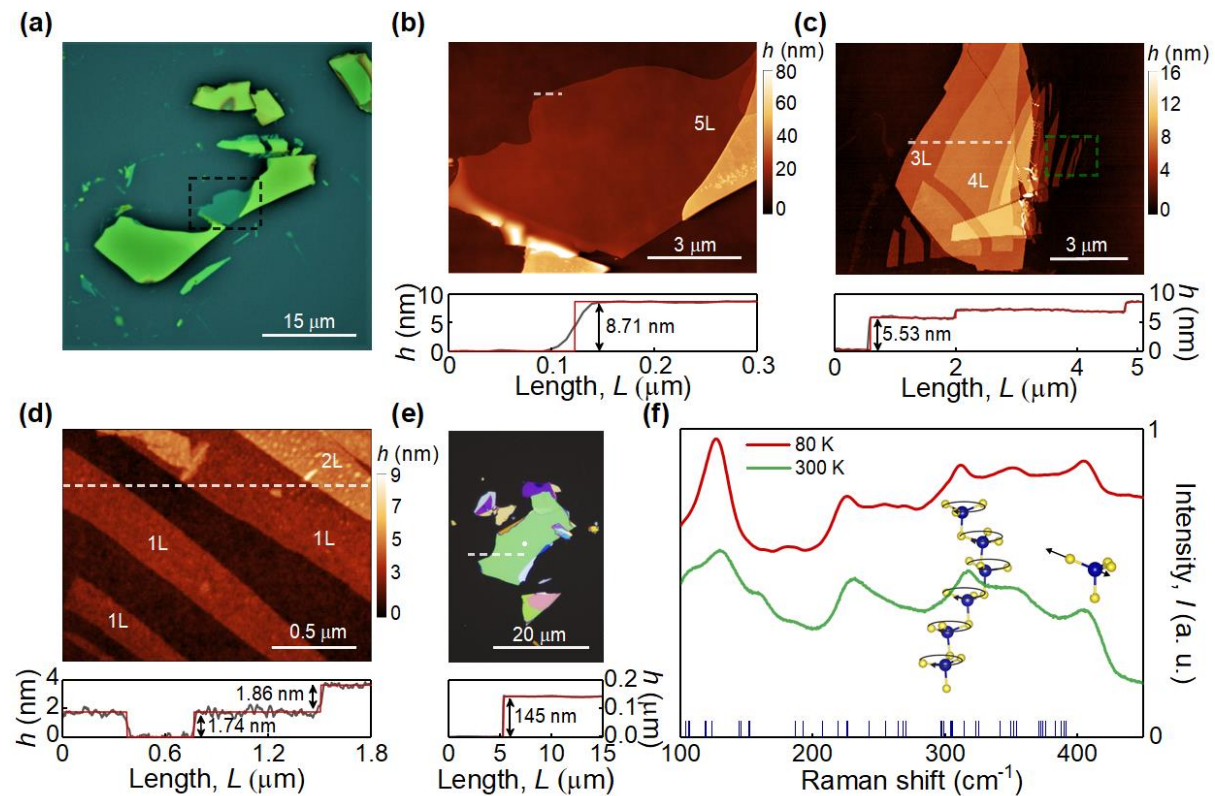


Figure 2: Cleavage feasibility of non-van der Waals InGaS₃. **a** 100X optical micrograph of a typical nanosheet on Si/SiO₂ substrate. **b** AFM topographical scan of atomic sheets over the region marked by dashed rectangle in (a). Height profiles are taken along dashed lines throughout the figure, thickness equivalent to 5L (8.71±0.38 nm). **c** Same as (b), but for thinner atomic sheets, thickness equivalent to 3L (5.53±0.32 nm) and 4L (7.3±0.34nm). **d** Same as (c), but a magnified region marked by a dashed rectangle in panel (c) and for atomic strips instead, thickness equivalent to 1L (1.74±0.24nm) and 2L (1.86±0.28nm). **e** 100X optical micrograph of typical nanosheet on a quartz substrate. White dot marks the Raman spectra collection point (145±4nm). **f** Raman spectra of the nanosheet presented in panel (e) at room (green line) and liquid nitrogen (red line) temperatures. Vertical bars label evaluated Raman-active modes (see Supplementary ST3 for details). Insets: Schematic representation of lattice vibration directions and corresponding Raman-active modes.

Figure 2 (f) shows Raman spectra of hexagonal InGaS₃ nanosheets performed at room and liquid nitrogen temperatures. Obtained spectral profiles have a complex form due to the overlapping bands, although peaks are slightly sharper at lower temperatures. The profiles display deeps at wavenumbers of 180 - 200 cm⁻¹ and 270 - 290 cm⁻¹, which is in a good agreement with our lattice dynamics calculations (see vertical bars on the inset of Figure 2 (f)). Those predict an absence of vibrational modes within these wavenumber ranges (see Methods for calculation details). For hexagonal InGaS₃ in the P6₃ space group, there are 90 normal vibrational modes in the center of the first Brillouin zone. Those can be represented by the following expression $\Gamma_v = 15A + 15B + 15E_1 + 15E_2$. Here, $A + E_1$ are acoustical translational modes, B are the silent modes, $14A + 14E_1$ are infrared-active modes, while $14A + 14E_1 + 15E_2$ are Raman-active modes. Their wavenumbers at zero-pressure are presented in

Supplementary Table ST3. The contribution of individual atoms to vibrational modes - the partial phonon density of states (pPDoS), is presented in Supplementary Figure S4. According to our pPDoS evaluations, the strong peak at 125 cm^{-1} is a mixed vibration of Gallium and Indium atoms, while the weak shoulder at the low-wavenumber region (157 cm^{-1}) is related to Gallium translations. The middle range of the spectra (from 200 to 270 cm^{-1}) associates to Sulphur vibrations. The high-wavenumber spectral part, above 290 cm^{-1} , mostly associates with Ga-S vibrations. An example of Gallium-Sulphur stretching-like mode is shown in Figure 2 (f, right inset). For the tetrahedral GaS_4 combined in chains through common Sulphur atoms emerge specific rotational vibrations of structural units, for instance, those that are demonstrated in Figure 2 (f, mid inset). In this case, the rotation of triangle-like GaS_3 units is observed. Raman spectra of thinner, up to bilayer, sheets are provided in Supplementary Figure S5. Those show no apparent shift in peak positions and a generally expected decline in their amplitudes.

Anisotropic optical properties and crystal structure reckoning of non-van der Waals InGaS_3

We investigated the anisotropic dielectric tensor (Figure 3(a)) of hexagonal InGaS_3 through imaging spectroscopic ellipsometry in the tiny region of interest of $10\text{ }\mu\text{m}^2$ within the area of exfoliated sheets. The ability to focus on the homogeneous high-quality region is a key benefit of our imaging technology²⁴.

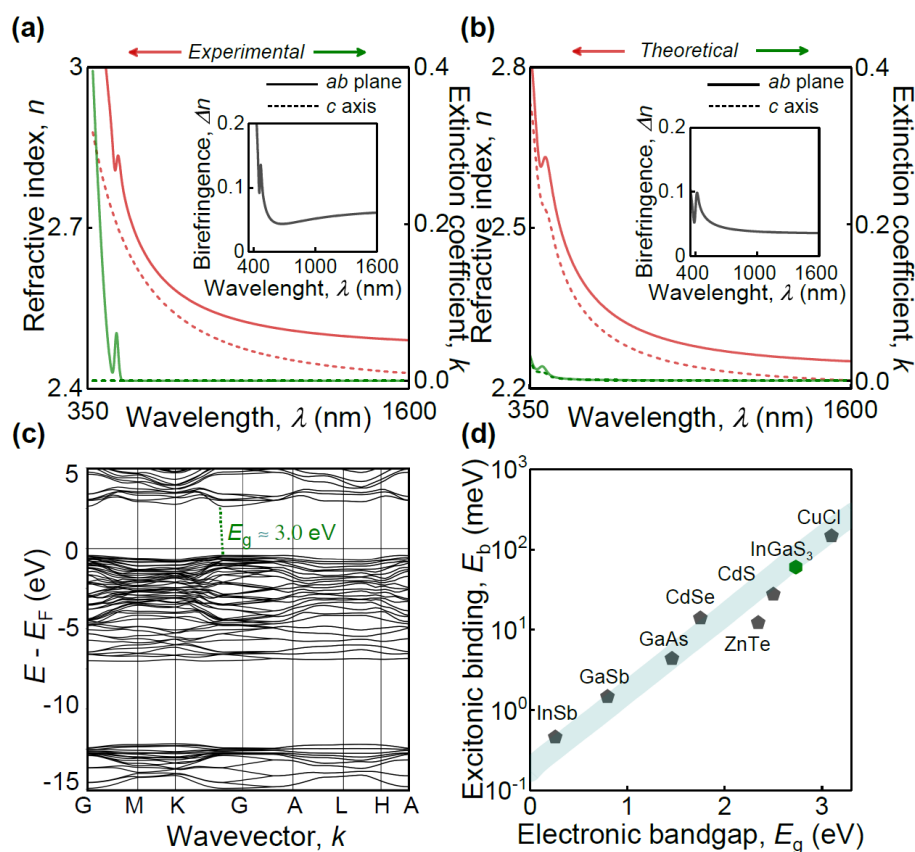


Figure 3: Non-van der Waals InGaS_3 optical response. **a** Experimental and **b** first-principle refractive indices and extinction coefficients for ab -plane (straight line) and c -axis (dashed line) of commensurate values and trends validating the hexagonal structure of InGaS_3 (see Figure 1(a) inset) and **d**). Insets: material's birefringence. **c** Electronic bandstructure from first-principle calculations. Fermi energy (E_F) is shifted to zero for clarity. Electronic bandgap is of $E_g = 3\text{ eV}$. **d** Excitonic binding energy versus electronic bandgap in traditional semiconductor materials

Furthermore, we simultaneously recorded and analysed optical responses from four InGaS₃ sheets to ensure a great precision and reproducibility of our results (see Methods and Supplementary Information for details). The dielectric function of hexagonal InGaS₃, similarly to transition metal dichalcogenides, is best represented by Tauc-Lorentz oscillators^{25,26} and Cauchy model²⁷ across the crystallographic *ab*-plane and *c*-axis, respectively. Despite this, the non-van der Waals interaction reduces InGaS₃ birefringence to a relatively small value of $\Delta n \sim 0.1$ (the inset in Figure 3(a)) in contrast to the huge anisotropy of $\Delta n \sim 1.5$ in transition metal dichalcogenides with natural van der Waals bonds²⁴. To explain this relatively weak anisotropy, we have performed additional DFT calculations (see Figure 3 (b)). The comparison of plots in Figure 3 (a and b) reveals a good agreement between experimental and theoretical results. Furthermore, our evaluations confirm the crystal structure of InGaS₃ (see inset of Figure 1(a)) since dielectric response is a fingerprint of the material's electronic bandstructure (see Supplementary Information for details). We also evaluated optical constants for the orthorhombic phase of InGaS₃ predicted theoretically in recent work²⁰. Obtained constants are presented in Supplementary Figure S7. Those fail to successfully reproduce obtained experimental results. Hence, our technique, which combines a spectroscopic ellipsometry with density functional calculations unambiguously confirms the hexagonal structure of InGaS₃ in addition to the X-ray analysis, and can be potentially used for the identification of crystal structures of other materials.

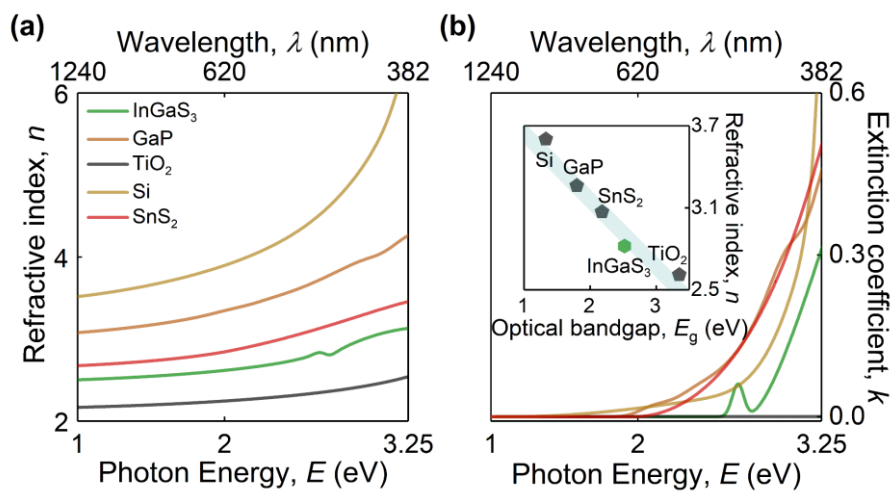


Figure 4: Towards visible-range all-dielectric nanophotonics with non-van der Waals InGaS₃. **a** Refractive index and **b** extinction coefficient spectra of visible-range high-refractive index and low-loss materials. Inset: The correlation between refractive indices and optical bandgaps for high-refractive index materials.

Apart from optical constants, we also evaluated the electronic bandstructure of hexagonal InGaS₃ (Figure 3(c)) and individual orbital-resolved density of electronic states (see Supplementary Figure S7) using the Heyd-Scuseria-Ernzerhof hybrid functional (see Methods)²⁸. For the latter, the main contributions to the bottom of conduction bands come from *s*-states of Gallium, Indium, and *p*-states of Sulphur atoms. From Figure 3(c), we conclude that InGaS₃ is an indirect bandgap semiconductor with $E_g = 3.0$ eV, which is close to bandgap ($E_g = 2.73$ eV) obtained experimentally from ellipsometry analysis. Moreover, we observed an excitonic peak at $E_{exc} = 2.67$ eV (464 nm) in optical response of the material, which is shown in Figure 3 (a). Its excitonic binding energy is $E_b = E_g - E_{exc} = 60$ meV. Interestingly, these values ($E_g = 2.73$ eV and $E_b = 60$ meV) are in line with bandgaps and excitonic binding energies of traditional semiconductors (Figure 3(d)). This indicates that the exciton in InGaS₃ has the same physical origin and thus can be described by Wannier-Mott model²⁹.

Finally, we would like to highlight the strong dielectric response of InGaS₃ (Figure 4(a)). Its refractive index is comparable to indices of classical high-index materials, such as silicon (Si)³⁰ and titanium oxide (TiO₂)^{31,32}, as well as recently emerging high-index materials, such as Gallium Phosphide (GaP)³³ and tin(IV) Sulphide (SnS₂)³⁴, as shown in Figure 4(a). More importantly, InGaS₃ has zero optical losses up to 2.57 eV (485 nm), as can be seen in Figure 4(b). This value lies between optical bandgaps of SnS₂ ($E_g = 2.18$ eV) and TiO₂ ($E_g = 3.35$ eV). Hence, InGaS₃ covers an important gap in visible spectral range for high-refractive index materials (see inset in Figure 4(b)). As a result, we conclude that it is an outstanding material for the novel research direction of all-dielectric meta-optics in the visible range^{33,35}.

Discussion

To sum up, we demonstrated that hexagonal InGaS₃ can be cleaved down to thicknesses of artificially created individual monolayers due to delicate and weak non-van der Waals bonds within its unit cell. It is made possible due to a specific arrangement of atoms across the crystallographic *c*-axis, where the exfoliation energy diminishes to 53 meVÅ⁻² for a selected atomic plane. This exfoliation energy value is within the range of conventional van der Waals materials. Furthermore, the hexagonal InGaS₃ is well suited for next-generation nanophotonics, mie-tronics³⁶, and expands high-refractive index palette³⁷. In particular, it meets two major requirements of miertonics: high-refractive index ($n > 2.5$) and broadband transparency ($k \approx 0$ above 465 nm). Its refractive index is about ~10% higher than of traditional TiO₂³⁸. Hence, all-dielectric nanostructures, such as waveguides³⁹, Mie-resonance nanoparticles⁴⁰, and subwavelength metasurfaces⁴¹ based on InGaS₃ should be ~10% more effective and compact. Additionally, it exhibits an out-of-plane optical anisotropy ($\Delta n \sim 0.1$), in contrast to conventional high-refractive index materials, which may greatly extend its scope of applications. Therefore, InGaS₃ possesses a unique combination of optical properties, such as high-refractive index, zero optical losses and out-of-plane anisotropy also offering convenient thickness control due to its structural properties.

Methods

X-ray crystallography. X-ray diffraction analysis of InGaS₃ single crystals was performed on Bruker D8 QUEST diffractometer with Photon III CMOS detector using Mo *K* α radiation ($\lambda = 0.71073$ Å) focused by multilayer Montel mirror. The full dataset was collected at the temperature of 100 K within ω -scans indexed with cell-now. It was integrated through SAINT from the SHELXTL PLUS package⁴². Absorption correction was completed by a multiscan approach implemented from SADABS⁴³. The crystal structure was solved by direct methods and refined anisotropically with full-matrix F^2 least-squares technique using SHELXTL PLUS package. The structure was refined in a chiral P6₅ space group with the resulting Flack parameter of 0.06 (2) being close to zero⁴⁴. The second virtual inversion twin-component was added to refinement by TWIN/BASF instruction to account for the absolute structural parameter. This led to a slight reduction of *R*-value from 2.50 % to 2.49 %. CSD reference number 2145523 contains supplementary crystallographic data for this manuscript. It can be obtained free of charge from Cambridge Crystallographic Data Centre via www.ccdc.cam.ac.uk/data_request/cif.

Density functional theory. Calculations of electronic bandstructure and optical constants were performed using the Vienna ab-initio simulation package VASP^{45,46} within generalized gradient approximation (GGA)⁴⁷. The Heyd-Scuseria-Ernzerhof (HSE) hybrid functional⁴⁸ in combination with

Perdew-Burke-Ernzerhof (PBE)⁴⁹ potentials was applied for accurate description of the electronic bandstructure. Electron-ion interactions were described by projector-augmented wave (PAW) method^{49,50}. The cutoff energy for the plane-wave basis set was set to 400 eV. The first Brillouin zone of the supercells was sampled with a 6×6×3 Monkhorst-Pack mesh⁵¹ of *k*-points for bulk supercell and 6×6×1 for monolayer case. The maximal force convergence tolerance settings for geometry optimization was set to 0.01 eVÅ⁻¹.

Lattice dynamics calculations. First principle lattice dynamics calculations were carried out with the CASTEP code package⁵². The crystal structure was fully optimized using LD approximation with CA-PZ exchange-correlation functional based on Ceperley and Alder numerical representation⁵³ parameterized by Perdew and Zunger⁵⁴. Maximal force and stress tensor convergence tolerance settings for geometry optimization were set to 0.01 eVÅ⁻¹ and 0.02 GPa, respectively. 5s₂ 5p₁, 3d₁₀ 4s₂ 4p₁, and 3s₂ 3p₄ orbitals were considered occupied with valence electrons for Indium, Gallium and Sulphur, respectively. Plane-wave cutoff energy was set to 880 eV for 4×4×2 sampling of the first Brillouin zone by the Monkhorst-Pack method.

Atomic Force Microscopy. The thickness and surface morphology of InGaS₃ sheets were accurately characterized by an atomic force microscope (NT-MDT Ntegra II) operated in a HybriD mode at ambient conditions. AFM images were acquired using silicon tips from TipsNano (GOLDEN, NSG 10) with spring constant of 11.8 N/m, head curvature radius < 10 nm, and resonant frequency of 240 kHz. The measurements were performed at a scan rate of 0.3 Hz and 512 pixel resolution. The obtained datasets were analyzed by the Gwyddion software.

Imaging spectroscopic ellipsometry. To analyze anisotropic optical response of InGaS₃, we used commercial imaging spectroscopic ellipsometer Accurion nanofilm_ep4 in the nulling mode. Ellipsometry spectra were recorded for four sheets with various thicknesses (*h* = 3.6 nm, 68.5 nm, 103.0 nm, and 277.4 nm) in the spectral range from ultraviolet (360 nm) to near-infrared (1700 nm). For ellipsometry analysis, we followed the algorithm described in Supplementary Note 2 of our recent work²⁴.

Supplementary Information

Supplementary material contains extra characterization results of non-van der Waals InGaS₃ sheets by a variety of techniques: energy-dispersive X-ray analysis, Raman spectroscopy, transmission electron diffraction patterns, AFM scans of inhomogeneous ultrathin sheets. It incorporates the summary data on X-ray diffraction patterns, and includes first-principle evaluation of optical constants along with CASTER calculations of Raman-active modes for recently reported²⁰ orthorhombic phase of InGaS₃.

Acknowledgements

This work was supported by Russian Science Foundation (No. 21-79-00218).

References

1. Frisenda, R., Niu, Y., Gant, P., Muñoz, M. & Castellanos-Gomez, A. Naturally occurring van der Waals materials. *npj 2D Materials and Applications* vol. 4 (2020).
2. Velický, M. *et al.* Exfoliation of natural van der Waals heterostructures to a single unit cell

- thickness. *Nat. Commun.* **8**, 14410 (2017).
3. Geim, A. K. & Grigorieva, I. V. Van der Waals heterostructures. *Nature* **499**, 419–425 (2013).
 4. 2D Materials and Van der Waals Heterostructures. *MDPI Books*
<https://www.mdpi.com/books/pdfview/book/2437> doi:10.3390/books978-3-03928-769-7.
 5. Bonaccorso, F. *et al.* Graphene, related two-dimensional crystals, and hybrid systems for energy conversion and storage. *Science* **347**, 1246501 (2015).
 6. Ferrari, A. C. *et al.* Science and technology roadmap for graphene, related two-dimensional crystals, and hybrid systems. *Nanoscale* **7**, 4598–4810 (2015).
 7. Novoselov, K. S., Mishchenko, A., Carvalho, A. & Castro Neto, A. H. 2D materials and van der Waals heterostructures. *Science* **353**, aac9439 (2016).
 8. Mounet, N. *et al.* Two-dimensional materials from high-throughput computational exfoliation of experimentally known compounds. *Nat. Nanotechnol.* **13**, 246–252 (2018).
 9. Choudhary, K., Kalish, I., Beams, R. & Tavazza, F. High-throughput Identification and Characterization of Two-dimensional Materials using Density functional theory. *Sci. Rep.* **7**, 5179 (2017).
 10. Björkman, T., Gulans, A., Krasheninnikov, A. V. & Nieminen, R. M. van der Waals bonding in layered compounds from advanced density-functional first-principles calculations. *Phys. Rev. Lett.* **108**, 235502 (2012).
 11. Serles, P. *et al.* Friction of magnetene, a non-van der Waals 2D material. *Science Advances* **7**, eabk2041 (2021).
 12. Jin, C. & Kou, L. Two-dimensional non-van der Waals magnetic layers: functional materials for potential device applications. *J. Phys. D Appl. Phys.* **54**, 413001 (2021).
 13. Puthirath Balan, A. *et al.* A Non-van der Waals Two-Dimensional Material from Natural Titanium Mineral Ore Ilmenite. *Chem. Mater.* **30**, 5923–5931 (2018).
 14. Friedrich, R., Ghorbani-Asl, M., Curtarolo, S. & Krasheninnikov, A. V. Data-Driven Quest for Two-Dimensional Non-van der Waals Materials. *Nano Lett.* **22**, 989–997 (2022).
 15. Puthirath Balan, A. *et al.* Exfoliation of a non-van der Waals material from iron ore hematite. *Nat. Nanotechnol.* **13**, 602–609 (2018).
 16. Peng, J. *et al.* Stoichiometric two-dimensional non-van der Waals AgCrS₂ with superionic behaviour at room temperature. *Nat. Chem.* **13**, 1235–1240 (2021).
 17. Zhao, S. Y. F. *et al.* Sign-Reversing Hall Effect in Atomically Thin High-Temperature Bi₂.1Sr₁.9CaCu₂.008 δ Superconductors. *Physical Review Letters* vol. 122 (2019).
 18. Bandyopadhyay, A., Frey, N. C., Jariwala, D. & Shenoy, V. B. Engineering Magnetic Phases in Two-Dimensional Non-van der Waals Transition-Metal Oxides. *Nano Lett.* **19**, 7793–7800 (2019).
 19. Puthirath, A. B. *et al.* Apparent Ferromagnetism in Exfoliated Ultrathin Pyrite Sheets. *J. Phys. Chem. C* **125**, 18927–18935 (2021).
 20. Chen, W. *et al.* Anomalous layer-dependent electronic and piezoelectric properties of 2D GaInS₃ nanosheets. *Appl. Phys. Lett.* **118**, 213103 (2021).
 21. *Inorganic Materials*. (Consultants Bureau, 1987).
 22. Flack, H. D. & Bernardinelli, G. The use of X-ray crystallography to determine absolute configuration. *Chirality* **20**, 681–690 (2008).
 23. Jung, J. H., Park, C.-H. & Ihm, J. A Rigorous Method of Calculating Exfoliation Energies from First Principles. *Nano Lett.* **18**, 2759–2765 (2018).
 24. Ermolaev, G. A. *et al.* Giant optical anisotropy in transition metal dichalcogenides for next-generation photonics. *Nat. Commun.* **12**, 854 (2021).
 25. Ermolaev, G. A., Yakubovsky, D. I., Stebunov, Y. V., Arsenin, A. V. & Volkov, V. S. Spectral ellipsometry of monolayer transition metal dichalcogenides: Analysis of excitonic peaks in dispersion. *Journal of Vacuum Science & Technology B* vol. 38 014002 (2020).
 26. Ermolaev, G. *et al.* Topological phase singularities in atomically thin high-refractive-index materials. *Nat. Commun.* **13**, 2049 (2022).

27. Tompkins, H. G. & Hilfiker, J. N. *Spectroscopic Ellipsometry: Practical Application to Thin Film Characterization*. (2015).
28. Heyd, J., Scuseria, G. E. & Ernzerhof, M. Hybrid functionals based on a screened Coulomb potential. *The Journal of Chemical Physics* vol. 118 8207–8215 (2003).
29. Haug, H. & Koch, S. W. Quantum Theory of the Optical and Electronic Properties of Semiconductors. (1993) doi:10.1142/1977.
30. Herzinger, C. M., Johs, B., McGahan, W. A., Woollam, J. A. & Paulson, W. Ellipsometric determination of optical constants for silicon and thermally grown silicon dioxide via a multi-sample, multi-wavelength, multi-angle investigation. *Journal of Applied Physics* vol. 83 3323–3336 (1998).
31. Tiwald, T. E. & Schubert, M. Measurement of rutile TiO₂ dielectric tensor from 0.148 to 33 μm using generalized ellipsometry. *SPIE Proceedings* (2000) doi:10.1117/12.403587.
32. Ermolaev, Ermolaev, Kushnir, Sapoletova & Napolskii. Titania Photonic Crystals with Precise Photonic Band Gap Position via Anodizing with Voltage versus Optical Path Length Modulation. *Nanomaterials* vol. 9 651 (2019).
33. Khmelevskaia, D. *et al.* Directly grown crystalline gallium phosphide on sapphire for nonlinear all-dielectric nanophotonics. *Applied Physics Letters* vol. 118 201101 (2021).
34. Ermolaev, G. A. *et al.* Broadband Optical Constants and Nonlinear Properties of SnS₂ and SnSe₂. *Nanomaterials* vol. 12 141 (2021).
35. Kruk, S. & Kivshar, Y. Functional Meta-Optics and Nanophotonics Governed by Mie Resonances. *ACS Photonics* vol. 4 2638–2649 (2017).
36. Kivshar, Y. The Rise of Mie-tronics. *Nano Lett.* (2022) doi:10.1021/acs.nanolett.2c00548.
37. Khurgin, J. B. Expanding the Photonic Palette: Exploring High Index Materials. *ACS Photonics* **9**, 743–751 (2022).
38. Dorrah, A. H., Rubin, N. A., Tamagnone, M., Zaidi, A. & Capasso, F. Structuring total angular momentum of light along the propagation direction with polarization-controlled meta-optics. *Nat. Commun.* **12**, 6249 (2021).
39. Hu, F. *et al.* Imaging exciton–polariton transport in MoSe₂ waveguides. *Nat. Photonics* **11**, 356–360 (2017).
40. Tselikov, G. I. *et al.* Transition metal dichalcogenide nanospheres for high-refractive-index nanophotonics and biomedical theranostics. *arXiv [physics.optics]* (2021).
41. Dorrah, A. H. & Capasso, F. Tunable structured light with flat optics. *Science* **376**, eabi6860 (2022).
42. Sheldrick, G. M. SHELXTL v. 5.10, Structure Determination Software Suite, Bruker AXS, Madison (Wisconsin, USA). (1998).
43. Sheldrick, G. M. (1998a). SADABS v. 2.01, Bruker/Siemens Area Detector Absorption Correction Program, Bruker AXS, Madison, Wisconsin, USA. (1998).
44. Flack, H. D. & Bernardinelli, G. Absolute structure and absolute configuration. *Acta Crystallogr. A* **55**, 908–915 (1999).
45. Kresse, G. & Furthmüller, J. Efficient iterative schemes for ab initio total-energy calculations using a plane-wave basis set. *Phys. Rev. B Condens. Matter* **54**, 11169–11186 (1996).
46. Kresse, G. & Joubert, D. From ultrasoft pseudopotentials to the projector augmented-wave method. *Phys. Rev. B Condens. Matter* **59**, 1758–1775 (1999).
47. Zhang, Y. & Yang, W. Comment on ‘Generalized Gradient Approximation Made Simple’. *Phys. Rev. Lett.* **80**, 890–890 (1998).
48. Heyd, J. & Scuseria, G. E. Efficient hybrid density functional calculations in solids: Assessment of the Heyd–Scuseria–Ernzerhof screened Coulomb hybrid functional. *J. Chem. Phys.* **121**, 1187–1192 (2004).
49. Perdew, J. P., Burke, K. & Ernzerhof, M. Generalized Gradient Approximation Made Simple. *Phys. Rev. Lett.* **77**, 3865–3868 (1996).
50. Blöchl, P. E., Först, C. J. & Schimpl, J. Projector augmented wave method: ab initio molecular

- dynamics with full wave functions. *Bulletin of Materials Science* vol. 26 33–41 (2003).
51. Monkhorst, H. J. & Pack, J. D. Special points for Brillouin-zone integrations. *Phys. Rev. B Condens. Matter* **13**, 5188–5192 (1976).
 52. Clark, S. J. *et al.* First principles methods using CASTEP. *Zeitschrift für Kristallographie - Crystalline Materials* **220**, 567–570 (2005).
 53. Ceperley, D. M. & Alder, B. J. Ground State of the Electron Gas by a Stochastic Method. *Phys. Rev. Lett.* **45**, 566–569 (1980).
 54. Perdew, J. P. & Zunger, A. Self-interaction correction to density-functional approximations for many-electron systems. *Phys. Rev. B Condens. Matter* **23**, 5048–5079 (1981).